Precipitation strengthening in Mg-Sn alloys with multiple precipitate types

Lyu, Yang; Jones, Ian P.; Chiu, Yu Lung

DOI:
10.1080/14786435.2022.2079749

Precipitation strengthening in Mg-Sn alloys with multiple precipitate types

Yang Lyu, Ian. P. Jones, Yu-Lung Chiu,
School of Metallurgy and materials, University of Birmingham, Birmingham, United Kingdom, B15 2TT

Abstract

Peak-aged Mg-6Sn, Mg-6Sn-3Al and Mg-6Sn-3Zn (wt.%) alloys have been characterised mechanically using micro-pillar compression and microstructurally using TEM. These alloys contain more than one type of precipitate. A modified Orowan equation is proposed to quantify the strengthening behaviour of the containing multiple precipitate types. The as-estimated values agree adequately with the experimental results.

1 Introduction

Magnesium alloys have attracted wide attention for their high specific strength. The most commonly applied Mg alloy system is the AZ series, which is a precipitation hardenable alloy strengthened by an $Mg_{17}(Al,Zn)_{12}$ phase. Due to the low melting point of the $Mg_{17}(Al,Zn)_{12}$ phase, AZ series alloys do not possess reliable properties at elevated temperatures[1]. The Mg-RE series alloys, on the other hand, have better performance at elevated temperatures due to a much better resistance to grain boundary sliding, which contributes 80% of the creep deformation[2], [3]. The high cost of rare earth elements, however, has limited the application of Mg-RE systems. The Mg-Sn alloy system also possesses reasonable performance at elevated temperature and is relatively low in cost[4]. Mg-Sn based alloys have the potential to provide a practicable alternative to Mg-RE in certain circumstances.

Mg_2Sn phase (fluorite structure, space group $Fm\bar{3}m$, a=0.674nm) with a melting point of ~770 ºC [5] is the main hardening phase in Mg-Sn alloys. This phase has complex morphologies and orientation relationships (OR) with the Mg matrix, depending on heat treatment and alloy composition[6]. In 1962, Henes and Gerold reported that 4 types of ORs exist in a Mg-3.75Sn (wt.%) binary alloy. OR1: $(110)_{Mg2Sn} \parallel (0001)_{Mg}, [001]_{Mg2Sn} \parallel [11\bar{2}0]_{Mg}$ and OR2: $(110)_{Mg2Sn} \parallel (0001)_{Mg}, [1\bar{1}1]_{Mg2Sn} \parallel [11\bar{2}0]_{Mg}$ appear

within the temperature range of 160 °C-200 °C, while OR3: $(111)_{Mg2Sn} \parallel (0001)_{Mg}, [2\bar{1}\bar{1}]_{Mg2Sn} \parallel [11\bar{2}0]_{Mg}$ and OR4: $(111)_{Mg2Sn} \parallel (0001)_{Mg}, [1\bar{1}0]_{Mg2Sn} \parallel [2\bar{1}\bar{1}0]_{Mg}$ appear at ageing temperatures from 200 °C to 300 °C. The habit planes of the precipitates also vary from $(0001)_{Mg}$ to $(10\bar{1}1)_{Mg}$ to $(10\bar{1}2)_{Mg}$ [7].

The competition between the different orientation relationships and habit planes of Mg_2Sn precipitates is quite complex. As summarized by Liu *et al.*, 14 types of orientation relationship had already been observed in different Mg-Sn alloys up until 2018[6]. As non-basal precipitates are expected to promote effectively resistance to basal slip, which is the most important deformation mechanism in Mg, formation of these precipitates in the Mg-Sn alloys is desirable[8], [9]. Various alloying attempts have been made to promote the formation of non-basal precipitates: for example, it has been widely reported that the addition of Zn promotes the formation of non-basal precipitates[10]–[13]. Although Al is not as popular as Zn as a ternary addition, Elsayed *et al.* and some others have reported that the addition of Al also leads to the formation of non-basal precipitates[14]–[16]. The reason that certain alloy elements are capable of promoting the formation of non-basal precipitates is not fully understood although some suggestions have been proposed. Liu *et al.* observed interphase boundary segregation of Zn in a Mg-Sn-Zn alloy and suggested that the presence of Zn may have altered the interfacial energy[17]. A phase-field simulation by Zhang *et al.* modelled the competition between chemical free energy and elastic strain energy and their respective effects on the phase transformation driving force. However, none of the above provides an adequate explanation of habit planes in Mg-Sn alloys.

Non-basal precipitates in Mg-Sn alloys are expected to block basal slip, but existing studies of the mechanical performance of Mg-Sn alloys either focused simply on hardness tests [11], [14], [18], [19], or employed macroscopic tensile tests on a polycrystal sample[10], [12], [20], [21]. The details of the deformation behaviour, on the other hand, are less well studied and the strengthening by non-basal precipitates, although this is predicted to be generally more effective than that of basal precipitates, has not been extensively analysed.

In this study, the basal slip behaviour of a binary Mg-6Sn (wt.%) alloy and ternary Mg-6Sn-3Al and Mg-6Sn-3Zn alloys has been analysed. Micro-pillar compression has been applied to analyse the effect of non-basal precipitates on basal slip. A general model based on the Orowan equation has been proposed to estimate the contribution to strength of the different precipitate types in Mg-Sn alloys.

2 Experimental

Three Mg-Sn alloys were prepared by sand-casting, with their nominal and actual chemical compositions (measured by SEM-EDS) listed in wt.% in Table 1. The raw materials used for casting were pure Mg (99.9%), pure Al (99.9%), pure Zn (99.9%) and pure Sn (99.95%). The ingots were cut into bars and solution treated at 500 ^{o}C for 48h in an argon filled quartz tube, to dissolve any precipitates and to homogenise the alloys. The samples were quenched into water and then aged at 200 ^{o}C until peak hardness was reached. The age hardening curves of the alloys were acquired using a Mitutoyo MVK-H1 Vickers hardness tester with a load of 50g. 10 measurements were recorded and averaged for each sample. For TEM analysis of the precipitates, samples were made by twin-jet polishing using a solution which consisted of 10g lithium chloride, 22g magnesium chloride, 200ml butoxyethanol and 1000ml methanol, used at -20 ^{o}C to -30 ^{o}C [22]. Some other TEM samples and the micro-pillars for compression experiments were prepared using an FEI Helios G4 C Xe plasma FIB. Microstructural observations were performed using an FEI Talos F200 TEM operated at 200kV and an FEI Tecnai F30 TEM operated at 300kV. The pillar compression experiments were carried out on an Alemnis indentation system installed in the Helios plasma FIB. Micro-pillars with a diameter of 10μm and a height of 20μm were prepared and compressed to a strain of 10% with a 10^{-3}/s strain rate.

Table 1 Nominal and actual chemical compositions of Mg-Sn alloys. The actual compositions were measured via SEM-EDX.

Alloy		Mg/wt.%	Sn/wt.%	Al/wt.%	Zn/wt.%	Others
Mg-6Sn	Nominal	94.00	6.00	0	0	Bal.
	Actual	93.47	6.25	0	0	
Mg-6Sn-3Al	Nominal	91.00	6.00	3.00	0	
	Actual	89.96	6.78	2.89	0	
Mg-6Sn-3Zn	Nominal	91.00	6.00	0	3.00	

	Actual	90.30	5.89	0	3.32	

3 Results

3.1 Age hardening response and microstructural characterisation

The 200 ˚C age hardening curves for the three Mg-Sn alloys are shown in Figure 1. The binary Mg-6Sn alloy did not reach a peak hardness within 300h whereas the other two alloys peaked at 72h ageing. The highest hardness value measured from the Mg-6Sn binary alloy was ~55±2HV, while the peak values of the Mg-6Sn-3Al alloy and the Mg-6Sn-3Zn alloy were ~70±3.5HV and ~72±1.5HV, respectively. Thus the increment of peak hardness for both ternary alloys compared with that measured from the binary Mg-6Sn is around 15HV.

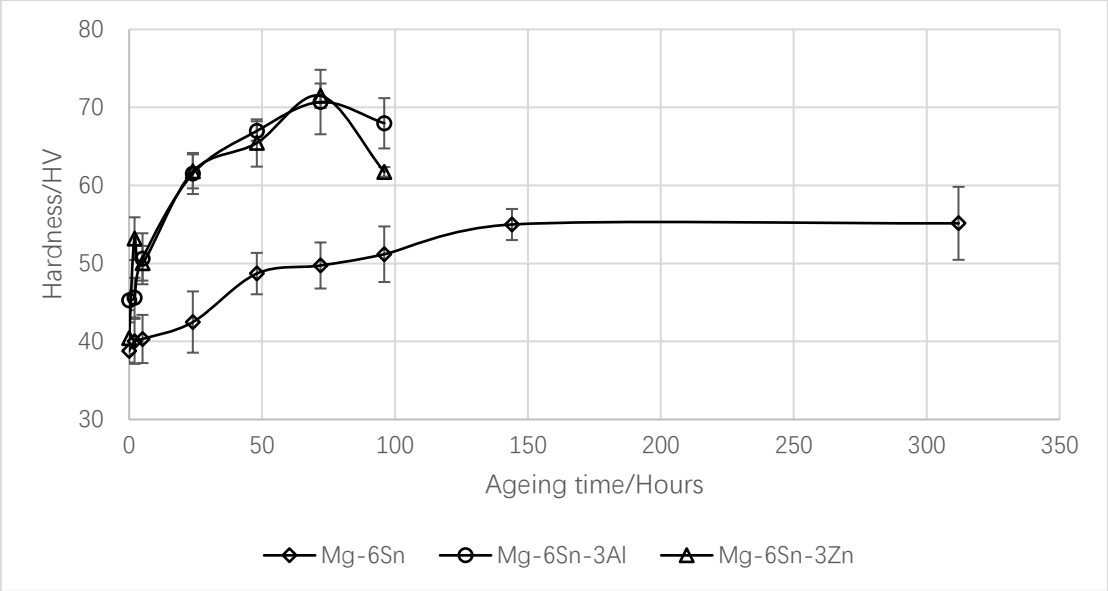

Figure 1 Vickers micro-hardness acquired from the Mg-Sn alloys with a 50g load

The precipitates in the Mg-6Sn, Mg-6Sn-3Al and Mg-6Sn-3Zn alloys were characterised by TEM. In the different alloys, the precipitates exhibit different morphologies and crystallography. TEM analysis has confirmed two types of Mg_2Sn precipitates in the Mg-6Sn alloy, four types of Mg_2Sn precipitate in the Mg-6Sn-3Al alloy and two types of Mg_2Sn and two types of $MgZn_2$ precipitate in the Mg-6Sn-3Zn alloy. The precipitate types, along with their morphologies and orientation relationships, are listed in Table 2. Statistics of the dimensions and percentage occurrences of various precipitate types can be found in Table 3, Table 4

and

Table 5. The detailed characterisation of the precipitates can be found in the supplementary material.

Table 2 Precipitate types and their respective morphologies and ORs in the three Mg-Sn alloys. The Mg_2Sn precipitates have been numbered

Alloy	Precipitate type	Morphology	OR
Mg-6Sn			
	Type 1	Basal lath with long axis along $\langle 11\bar{2}0\rangle_{Mg}$	$(0001)_{Mg} \parallel (110)_{Mg2Sn}, [11\bar{2}0]_{Mg} \parallel [001]_{Mg2Sn}$ (OR1)
	Type 2	Basal lath with long axis along $\langle 10\bar{1}0\rangle_{Mg}$	$(0001)_{Mg} \parallel (110)_{Mg2Sn}, [2\bar{1}\bar{1}0]_{Mg} \parallel [1\bar{1}1]_{Mg2Sn}$ (OR2)
Mg-6Sn-3Al			
	Type 3	Basal rod with long axis along $\langle 11\bar{2}0\rangle_{Mg}$	$(0001)_{Mg} \parallel (111)_{Mg2Sn}, [11\bar{2}0]_{Mg} \parallel [1\bar{1}0]_{Mg2Sn}$ (OR4)
	Type 4	Basal plate	
	Type 5	c-axis rod	
	Type 6	Pyramidal lath with a habit plane of $(1\bar{1}01)_{Mg}$	No specific OR
Mg-6Sn-3Zn			
	Type 2	Basal lath with long axis along $\langle 10\bar{1}0\rangle_{Mg}$	$(0001)_{Mg} \parallel (110)_{Mg2Sn}, [2\bar{1}\bar{1}0]_{Mg} \parallel [1\bar{1}1]_{Mg2Sn}$ (OR2)
	Type 7	Prismatic lath with long axis along $\langle 11\bar{2}0\rangle_{Mg}$	$(0001)_{Mg} \parallel (110)_{Mg2Sn}, [11\bar{2}0]_{Mg} \parallel [001]_{Mg2Sn}$ (OR1)
	$MgZn_2$ wide rod	c-axis rod	

	$MgZn_2$ narrow rod	c-axis rod	$(0001)_{Mg}$ ∥ $(11\bar{2}0)_{MgZn2}, [11\bar{2}0]_{Mg}$ ∥ $[10\bar{1}0]_{MgZn2}$

Table 3 Dimensions and percentage occurrences measured for the precipitates in the Mg-6Sn alloy

Precipitate type	Dimension	Average value/μm	Standard deviation	Percentage Occurrence
Type 1 basal lath	Length	0.888	0.27	21.70%
	Width	0.076	0.02	
	Thickness	0.059	0.01	
Type 2 basal lath	Length	0.700	0.17	78.30%
	Width	0.140	0.01	
	Thickness	0.069	0.02	

Table 4 Dimensions and percentage occurrences measured for the precipitates in the Mg-6Sn-3Al alloy

Precipitate type	Dimension	Value/μm	Standard deviation	Percentage occurrence
Type 3 basal rod	Length	1.131	0.28	48.10%
	Diameter	0.039	0.01	
Type 4 basal plate	Length	0.188	0.05	37.80%
	Width	0.118	0.04	
	Thickness	0.071	0.02	
Type 5 c-axis rod	Length	0.245	0.08	6.50%
	Diameter	0.072	0.02	
Type 6 pyramidal lath	Length	1.241	0.20	7.60%
	Width	0.169	0.07	
	Thickness	0.041	0.01	

Table 5 Dimensions and percentage occurrences measured for the precipitates in the Mg-6Sn-3Zn alloy.

The narrow MgZn2 rods are excluded as they do not participate in Orowan looping

Precipitate type	Dimension	Value/μm	Standard deviation	Percentage occurrence	Percentage occurrence without the $MgZn_2$ narrow rods
Type 2 basal lath	Length	0.391	0.08	10.50%	48.83%
	Width	0.136	0.03		
	Thickness	0.050	0.01		
Type 7 prismatic lath	Length	0.705	0.08	2.30%	10.70%
	Width	0.129	0.02		
	Thickness	0.079	0.02		
$MgZn_2$ wide rod	Length	0.322	0.12	8.70%	40.47%
	Diameter	0.070	0.02		
$MgZn_2$ narrow rod	Length	0.681	0.22	78.60%	
	Diameter	0.013	0.01		

3.2 Pillar compression tests

An example of a peak-aged Mg-6Sn pillar before and after compression is shown in Figure 2. The alloys, along with their respective loading directions and highest Schmid factors for basal slip, are listed in Table 6. The stress-strain curves for all three alloy samples are shown in Figure 3.

Table 6 Mg-Sn alloy micro-pillars with loading directions and highest Schmid factors for basal slip

Alloy	Loading direction	Schmid factor
Mg-6Sn	$[01\bar{1}1]_{Mg}$	0.4321
	$[\bar{1}2\bar{1}\bar{2}]_{Mg}$	0.4984

Mg-6Sn-3Al	$[\bar{1}3\bar{2}\bar{2}]_{Mg}$	0.4634
	$[\bar{1}8\bar{7}\bar{9}]_{Mg}$	0.4560
Mg-6Sn-3Zn	$[\bar{1}8\bar{7}\bar{6}]_{Mg}$	0.4397
	$[25\bar{7}6]_{Mg}$	0.4828

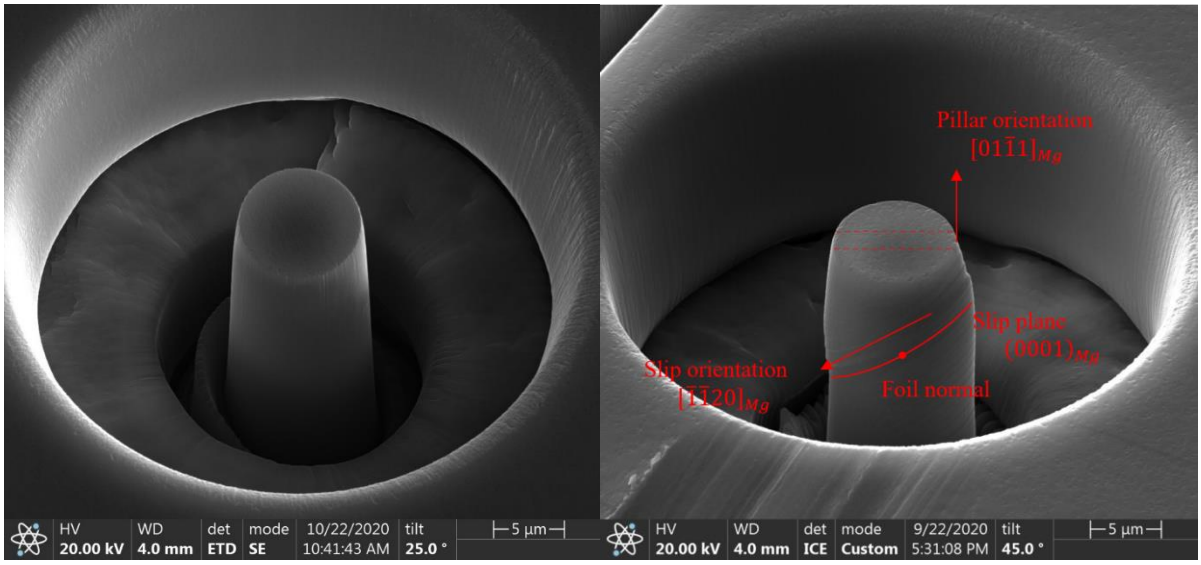

Figure 2 A Mg-6Sn micro-pillar (a) before and (b) after compression. For this specific sample, the TEM foil has a foil normal of $[1\bar{2}10]_{Mg}$

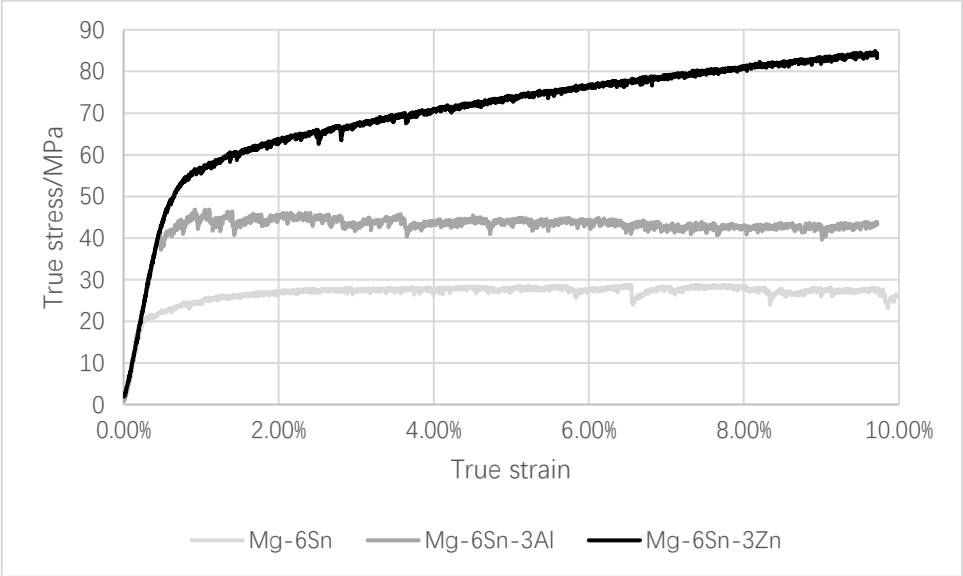

Figure 3 Three examples of stress-strain curves for the three Mg-Sn alloys. The respective loading directions for Mg-6Sn, Mg-6Sn-3Al and Mg-6Sn-3Zn are $[01\bar{1}1]_{Mg}$, $[\bar{1}3\bar{2}\bar{2}]_{Mg}$ and $[\bar{1}8\bar{7}\bar{6}]_{Mg}$

The yield strengths were measured as the 0.2% proof stresses. For Mg-6Sn, Mg-6Sn-3Al and Mg-6Sn-

3Zn, using the Schmid factors given above, the CRSSs for basal slip are 13.22 MPa, 21.34 MPa and 29.92 MPa. The slip planes and directions were identified by SEM; TEM specimens were FIB machined from the as-compressed pillars to confirm the slip system activated during compression and to analyse the interaction between precipitates and dislocations. The TEM images taken from the as-compressed pillars are shown in Figure 4. Dislocations can be seen in all three alloys. With $g = 0002$, no dislocations are visible in the samples. Dislocations appeared visible with $g = 10\bar{1}0$ or $g = 11\bar{2}0$ types. This confirms that the dislocations activated during the compression are basal <**a**> dislocations. For the Mg-6Sn and Mg-6Sn-3Al alloys, because no precipitate shearing was observed, Orowan looping is expected to be the dominating interaction mechanism between the precipitates and the dislocations. For the Mg-6Sn-3Zn alloy, shearing of the $MgZn_2$ precipitates *is* observed. Figure 5 shows a TEM image of the sheared precipitates. The slip bands have clearly penetrated the precipitates.

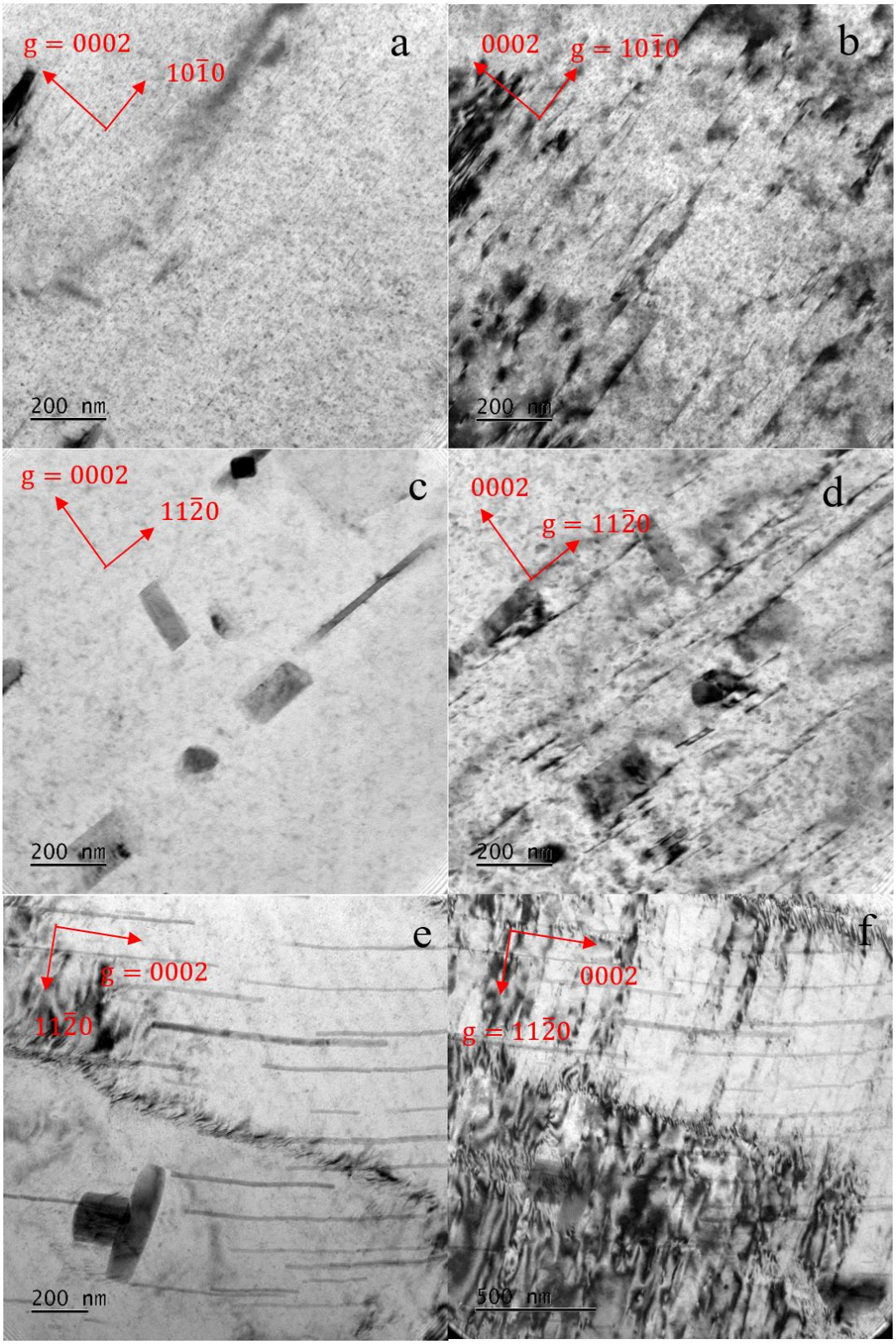

Figure 4 TEM images taken from the as-compressed Mg-Sn samples indicating invisibility and visibility of basal a dislocations: (a) dislocations invisible in Mg-6Sn, (b) dislocations visible in Mg-6Sn, (c) dislocations invisible in Mg-6Sn-3Al, (d) dislocations visible in Mg-6Sn-3Al, (e) dislocations invisible in Mg-6Sn-3Zn, (f) dislocations visible in Mg-6Sn-3Zn

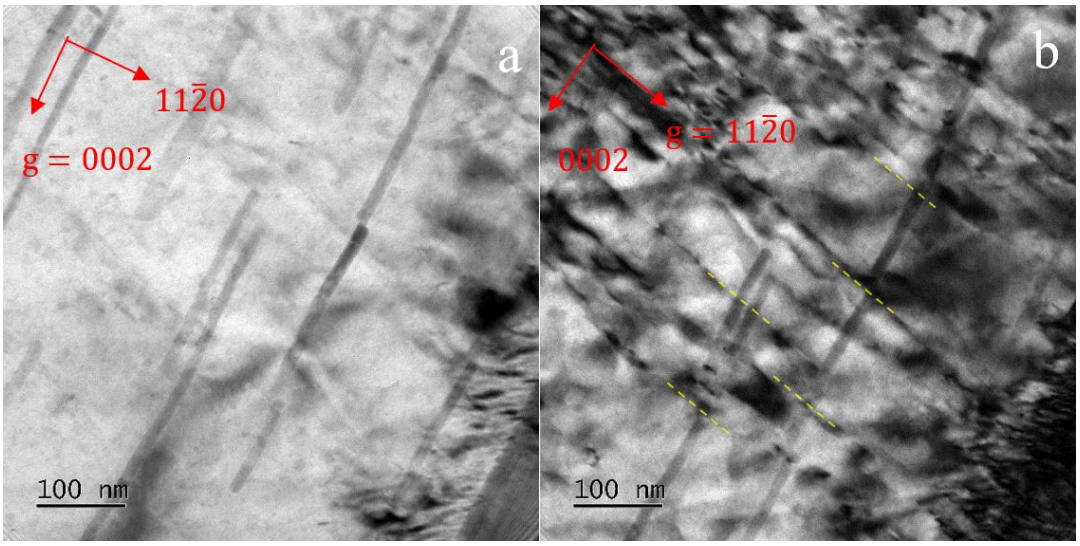

Figure 5 TEM image of sheared prismatic $MgZn_2$ precipitates viewed along $[1\bar{1}00]_{Mg}$ with (a) $g = 0002$ and (b) $g = 11\bar{2}0$. Dislocations are visible and penetrate the precipitates as marked by the dashed lines.

Although Orowan looping is expected to take place in all three alloys, dislocation loops were not observed in the samples using a series of different imaging conditions. This does not mean Orowan looping has not taken place. A simulation study by Vaid *et al.* of the $Mg_{17}Al_{12}$ precipitates suggests that Orowan loops may collapse into the matrix-precipitate interphase boundary and therefore become extinct[23]. Similar behaviour may have taken place in these Mg-Sn alloys.

3.3 Evaluation of Orowan strengthening

The increase in strength results mainly from the presence of non-basal precipitates and the increased number density of precipitates driven by micro-alloying. Generally, the strength provided by Orowan looping is straightforward to calculate using the Orowan strengthening equation:

$$\sigma_{Orowan} = \frac{MGb}{2\pi\sqrt{1-\nu}}\frac{1}{\lambda}\ln\left(\frac{d_p}{r_0}\right) \quad (1)$$

where M is the Taylor factor, G the shear modulus of Mg, b the Burgers vector of the dislocations, ν Poisson's ratio. λ and d_p are respectively the mean spacing and diameter of the particles in the slip plane and r_0 is the cut-off radius of the dislocation core and is normally taken equal to b [24]. Therefore, for a certain alloy system with a certain type of precipitate, Orowan strengthening will be straightforward to

quantify knowing λ and d_p.

For the Mg-Sn alloy systems, it is however complex to apply the general Orowan strengthening equation as multiple precipitate types are present. One particle spacing and particle size will not represent the various precipitate distributions in the system. Nie has developed a series of approaches of calculating λ based on different precipitate morphologies [25]. On this basis, λ for the basal plate precipitates and the c-axis rods observed in this study is then

$$\lambda = L_p - d_p = \frac{1.075}{\sqrt{N_A}} - \frac{\pi d_t}{4} = \left(\frac{0.779}{\sqrt{f}} - 0.785\right) d_t \quad (2)$$

Substituting this in the Orowan equation will give

$$\sigma_{Orowan} = \frac{Gb}{2\pi\sqrt{1-\nu}\left(\frac{0.779}{\sqrt{f}} - 0.785\right) d_t} \ln\frac{0.785 d_t}{b} \quad (3)$$

For the prismatic and pyramidal laths, λ will be

$$\lambda = L_p - \frac{d_p}{2} - \frac{\sqrt{3}t_p}{2} = 0.825\sqrt{\frac{d_t t_t}{f}} - 0.393 d_t - 0.866 t_t \quad (4)$$

Substituting in the Orowan equation

$$\sigma_{Orowan} = \frac{Gb}{2\pi\sqrt{1-\nu}\left(0.825\sqrt{\frac{d_t t_t}{f}} - 0.393 d_t - 0.866 t_t\right)} \ln\frac{0.886\sqrt{d_t t_t}}{b} \quad (5)$$

We use the total volume fraction of all precipitates in a specific Mg-Sn alloy, as this reflects the actual spacing between precipitates, regardless of their morphology. Then, a certain type of precipitate, when considering its contribution in isolation, contributes to the Orowan strengthening behaviour such that

$$\sigma_i = \sigma(d_i) = \frac{Gb}{2\pi\sqrt{1-\nu}} \frac{1}{\lambda} \ln\left(\frac{d_i}{r_0}\right) \quad (6)$$

With more than one type of precipitate present, the contribution of a specific precipitate type is determined by its respective fraction in the alloy, where

$$\sigma_i = \sigma(d_i, f_i) = \frac{f_i}{f} \frac{Gb}{2\pi\sqrt{1-\nu}} \frac{1}{\lambda} \ln\left(\frac{d_i}{r_0}\right) (7)$$

Therefore, the total contribution of all precipitate types in a certain alloy will be

$$\sigma_{Orowan} = \sum_{i=1}^{n} \sigma(d_i, f_i) = \sum_{i=1}^{n} \frac{f_i}{f} \frac{Gb}{2\pi\sqrt{1-\nu}} \frac{1}{\lambda} \ln\left(\frac{d_i}{r_0}\right) \quad (8)$$

This approach determines the mean particle spacing in a proper manner, and then weights the contribution of different precipitates by their respective volume fractions.

The size and number density of the precipitates were determined by TEM observations. The dimensions of the different types of precipitate can be found in Table 3, Table 4 and Table 5. The thicknesses of the TEM foils were measured by CBED and number densities can then be determined as 14.14/μm^3 for Mg-6Sn, 31.26/μm^3 for Mg-6Sn-3Al and 37.66/μm^3 for Mg-6Sn-3Zn. The overall volume fractions of precipitates in the different Mg-Sn alloys are therefore 8.95% for Mg-6Sn, 6.33% for Mg-6Sn-3Al and 9.23% for Mg-6Sn-3Zn ($MgZn_2$ narrow rods included).

Based on the approach explained above, the respective contributions of the different precipitate types, along with their overall contributions towards Orowan strengthening, can then be calculated. Using the precipitate dimensions measured by TEM, the calculation details of the various precipitate types are listed in Table 7:

Table 7 Orowan strengthening contribution of different precipitate types in Mg-Sn alloys

Alloy	Precipitate type	Volume fraction/%	Strength contribution/MPa
Mg-6Sn			
	Type 1	1.46%	0.59
	Type 2	7.49%	7.32
	Total	8.95%	7.91
	Experimental		13.22
Mg-6Sn-3Al			
	Type 3	2.15%	5.69
	Type 4	1.89%	3.79
	Type 5	0.19%	0.49
	Type 6	2.10%	5.65
	Total	6.33%	15.62
	Experimental		21.34
Mg-6Sn-3Zn			
	Type 2	4.54%	6.26
	Type 7	2.72%	4.24
	$MgZn_2$ wide rod	1.30%	2.75

	Total	8.56%	13.25
	Experimental		29.92

It can be found from the results that the Orowan strengthening contributions in the Mg-6Sn and Mg-6Sn-3Al alloys are around 75% that of the CRSSs measured experimentally. This is due to the strength of pure Mg and the strength from solid solution strengthening not being included in the calculation. For the Mg-6Sn-3Zn alloy, for example, the as-calculated strength is around half that of the actual CRSS.

In order to determine the total contributions of different strengthening mechanisms, solid solution strengthening and shearing of the $MgZn_2$ precipitates also need to be quantified. For solid solution strengthening, a widely applied approach is that of Caceres and Rovera [26]:

$$\sigma_s = CX^n \qquad (9)$$

where C is the solid solution strengthening rate with respect to solute concentration and n is either ½ or 2/3. The solid solution strengthening rate selected in this study is 13MPa/% for Sn, 9.9MPa/% for Al and 10.8MPa/% for Zn based on a few existing studies [26]–[29].

The chemical composition of the matrix was determined by TEM-EDS and is shown in Figure 6. Based on this matrix composition, the contributions to solid solution strengthening of the different elements in the three Mg-Sn alloys can then be calculated and are listed in Table 8.

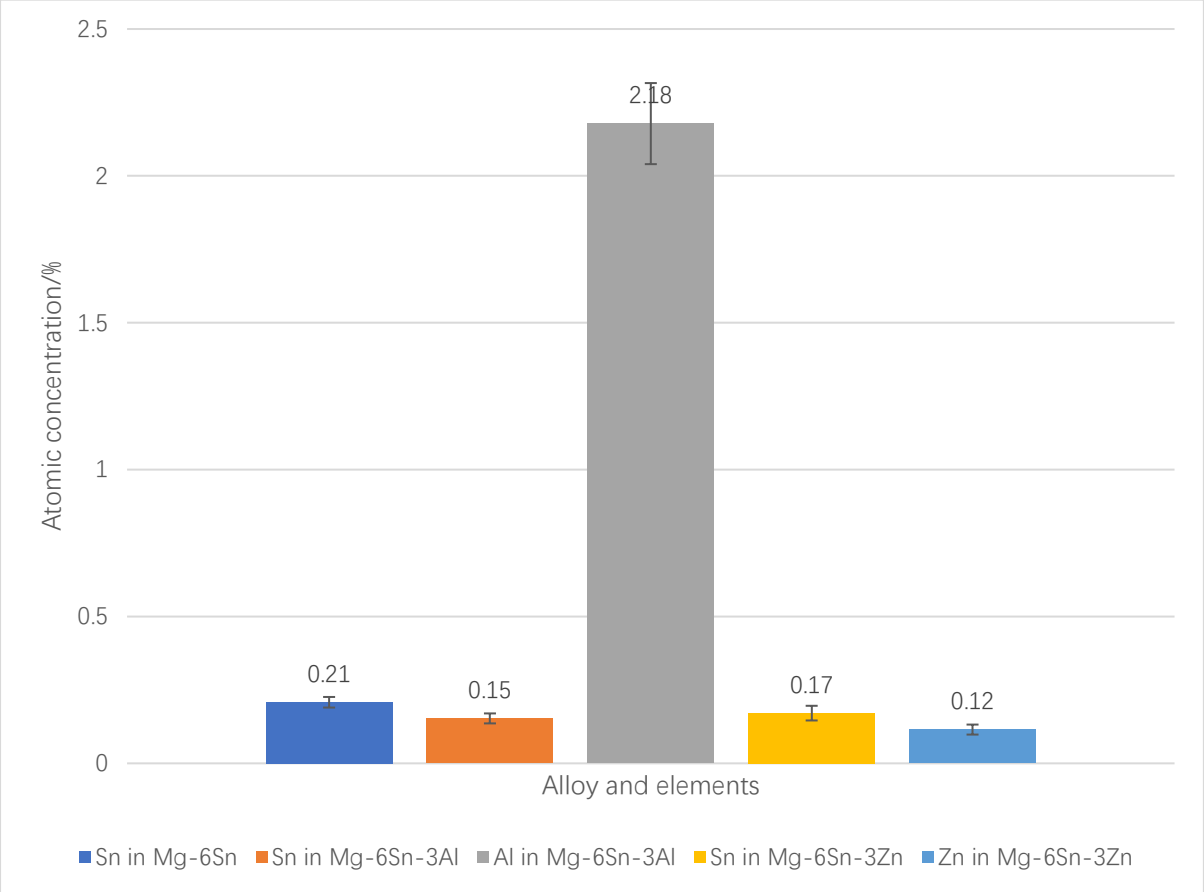

Figure 6 Atomic concentrations of alloying elements in the matrices of peak aged Mg-Sn alloys measured by STEM-EDS

Table 8 Contribution of basal slip CRSS from solid solution strengthening in Mg-Sn alloys

Solid solution strengthening contribution	Mg-6Sn/MPa	Mg-6Sn-3Al/MPa	Mg-6Sn-3Zn/MPa
Sn	1.66	1.49	1.55
Al		2.77	
Zn			1.18
Total	1.66	4.26	2.73

For the particle shearing, a simplified approach due to Schuh is applied to calculate the contribution of shearing towards strength [30]:

$$\Delta\tau_{APB} = \frac{\pi}{2b}\gamma_{APB}f \qquad (10)$$

where b is the magnitude of the Burgers vector, γ_{APB} is the anti-phase boundary energy and f is the volume fraction of the $MgZn_2$ narrow rods. The contribution of the shearing of the $MgZn_2$ narrow rods can then be calculated as 6.57MPa.

Therefore, based on all the calculations above, the strength contributions to basal slip in Mg-Sn alloys can be estimated and are listed in Table 9. The base CRSS of basal slip in pure Mg used here is 2MPa according to the existing literature [31], [28], [32], [33]:

Table 9 Total strength of basal slip in Mg-Sn alloys contributed by different strengthening mechanisms

Strengthening mechanism	Mg-6Sn/MPa	Mg-6Sn-3Al/MPa	Mg-6Sn-3Zn/MPa
Base strength	2		
Solid solution strengthening	1.66	4.26	2.73
Orowan strengthening	7.91	15.62	13.25
Particle shearing strengthening			6.57
Total	11.57	21.88	24.55
Experimental	13.22	21.34	29.92

For the Mg-6Sn and Mg-6Sn-3Al, the as-estimated strength has an adequate agreement with the experimentally measured strength. For the Mg-6Sn-3Zn alloy, the as-estimated strength is slightly lower than the actual strength. This could possibly be due to the stress accumulation effect and is discussed later.

4 Discussion

4.1 Shearing of $MgZn_2$ precipitates in the Mg-6Sn-3Zn alloy

It is generally accepted that the boundary between Orowan looping and precipitate shearing is determined by a critical particle size, where the dislocations tend to form a loop around the particles which are larger than the critical size and shear through the particles which are smaller than the critical size [34]. Currently, there are no experimental measures to determine this critical size in Mg alloys. Hutchinson

estimated the critical size by balancing the stress introduced by a bowed dislocation around the precipitate bent to a specific radius (normally taken as the precipitate size) R:

$$\frac{G_m b}{R} = \frac{G_p}{15} \qquad (11)$$

Based on this estimate, the critical size to shear the $Mg_{17}Al_{12}$ precipitates is around 3 nm [35]. For simplicity, this equation is applied directly to the Mg-Sn alloys in this study. For the Mg_2Sn precipitates in the Mg matrix, the critical size for particle shearing is 3.14 nm. For the $MgZn_2$ precipitates in the Mg matrix, the critical size for particle shearing is 2.74 nm. As all the precipitates in this work are larger than 20 nm, it is expected that all the precipitates in the three Mg-Sn alloys will not be sheared during the motion of basal **a** dislocations.

However, the actual experimental observation shows exactly the opposite results for the $MgZn_2$ precipitates. Most of the $MgZn_2$ precipitates were sheared, as shown previously in Figure 5, whereas the Mg_2Sn precipitates are not sheared. By measuring the distance that the precipitates have sheared, it can be estimated that ~150 dislocations have cut through the $MgZn_2$ precipitates after 10% compression strain.

Some recent studies also suggest that dislocations have sheared through precipitates that are obviously larger than the estimated critical size. Liao *et al.* predicted by computational modelling that the $Mg_{17}Al_{12}$ precipitates in AZ91 can be sheared by prismatic dislocations [36]. Cepeda-Jimenez *et al.* reported shearing of precipitates in AZ91 and Mg-11Nd (wt.%) alloys after tensile strain [37]. Solomon *et al.* reported β′ precipitates in Mg-Y alloys can be sheared by both basal **a** slip and **c** + **a** slip, while β‴ precipitates in Mg-Nd alloys can be sheared only by basal **a** slip [38]. A pillar compression study by Wang and Stanford reported the same $MgZn_2$ shearing behaviour in a Mg-5Zn (wt.%) alloy; they suggested that the shearing behaviour is probably due to good lattice parameter matching [39].

To explain the precipitate shearing, the overall precipitation sequence is reviewed here: at the beginning of precipitation, a structure which is rich in solute atoms, but maintaining the same crystal structure as the matrix, will appear. These precipitates are called G.P. zones [40]. The G.P. zone then develops into a phase with a new crystal structure which will begin to grow larger. During this process, the coherency of the precipitate-matrix interface will begin gradually to be destroyed. Due to the similarity of the structures of matrix and precipitate in the early stages of precipitation, certain dislocations tend to shear through the particles. When the size of the new particle exceeds a critical value, the remaining coherency of the interface will not sustain dislocation shearing which will therefore transfer to Orowan looping.

Hence, the essence of the transition from shearing to looping is influenced by the coherency of the interphase boundary. For the $MgZn_2$ precipitates in Mg-Sn alloys, the orientation relationship determined in this work is $[0001]_{Mg} \parallel [1\bar{2}10]_{MgZn2}$, $[10\bar{1}0]_{Mg} \parallel [0001]_{MgZn2}$, $[11\bar{2}0]_{Mg} \parallel [10\bar{1}0]_{MgZn2}$. On the $(1\bar{1}00)_{Mg} - (0001)_{MgZn2}$ interphase boundary, $[11\bar{2}0]_{Mg} \parallel [10\bar{1}0]_{MgZn2}$. Regarding the lattice parameter, there seems to be a large mismatch between the magnitude of $[11\bar{2}0]_{Mg}$ (3.19Å) and $[10\bar{1}0]_{MgZn2}$ (9.09Å). An image illustrating the orientation relationship between the Mg matrix and $MgZn_2$ precipitates viewed along $[0001]_{Mg} \parallel [1\bar{2}10]_{MgZn2}$ has been constructed using CrystalMaker[41] and is shown below in Figure 7.

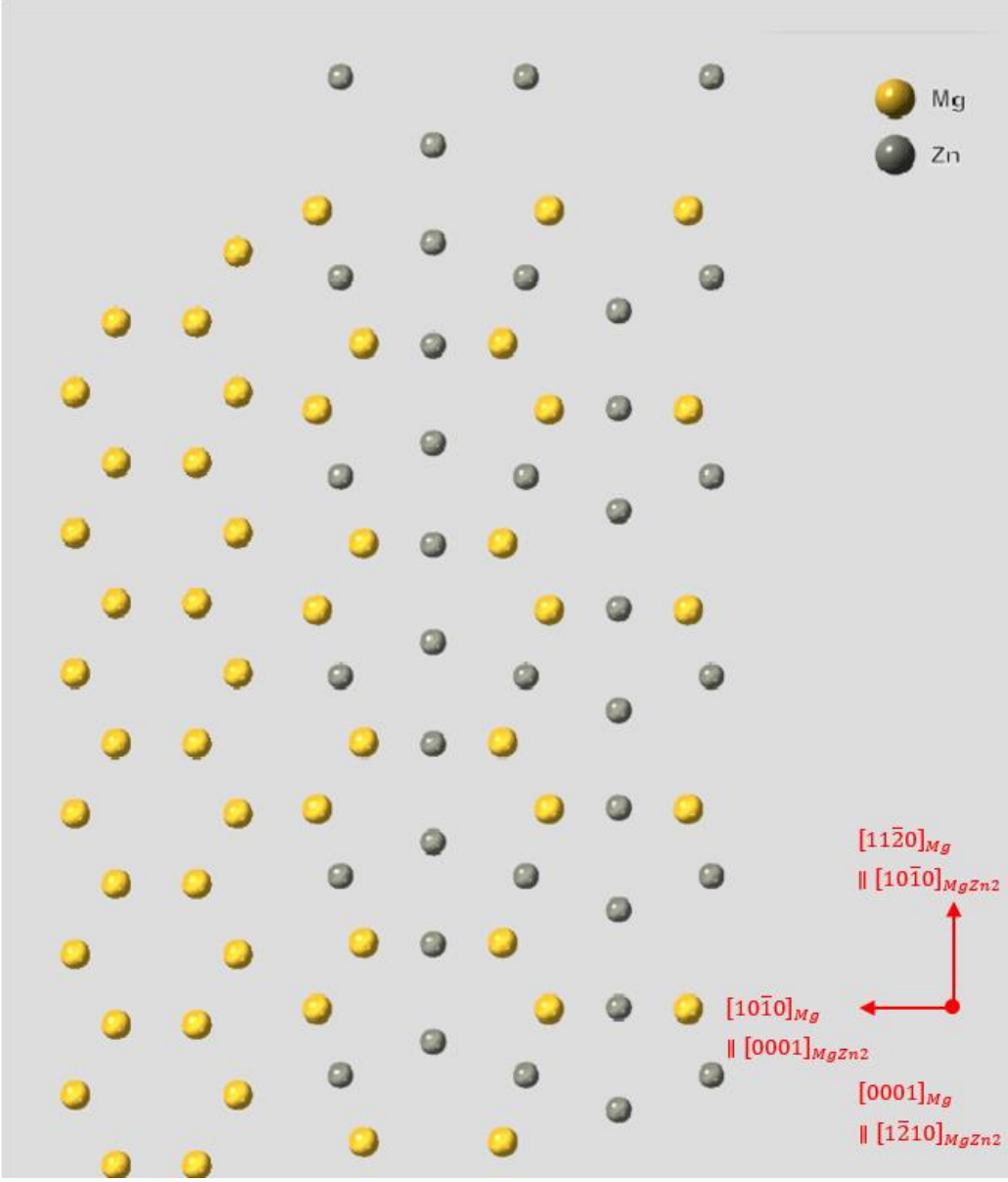

Figure 7 An illustration of the Mg-$MgZn_2$ interface reconstructed by CrystalMaker. Note the 2-D view of the crystal structure does not reflect the actual chemical composition of the $MgZn_2$ precipitate as some

atoms are obscured

However, the exact crystal structure of $MgZn_2$ reveals that there are two Mg atoms near the $(0001)_{MgZn2}$ plane which are close enough to be on the interphase boundary. With these two Mg atoms, the atom spacing along $[10\bar{1}0]_{MgZn2}$ will then reduce to 3.03Å, resulting in a good registry between the two structures. In this case, as the magnitude of the Burgers vector in the Mg matrix (~3.2 Å) will be close to that in the $MgZn_2$ (~3.03Å), this will lead to a semi-coherent, or even a constrained coherent interphase boundary with only 5.3% mismatch with the Mg matrix. An illustration of the similarity of crystal structures in the matrix (left column of atoms) and the precipitate (right column of atoms) in the $[11\bar{2}0]_{Mg} \parallel [10\bar{1}0]_{MgZn2}$ direction is shown below in Figure 8.

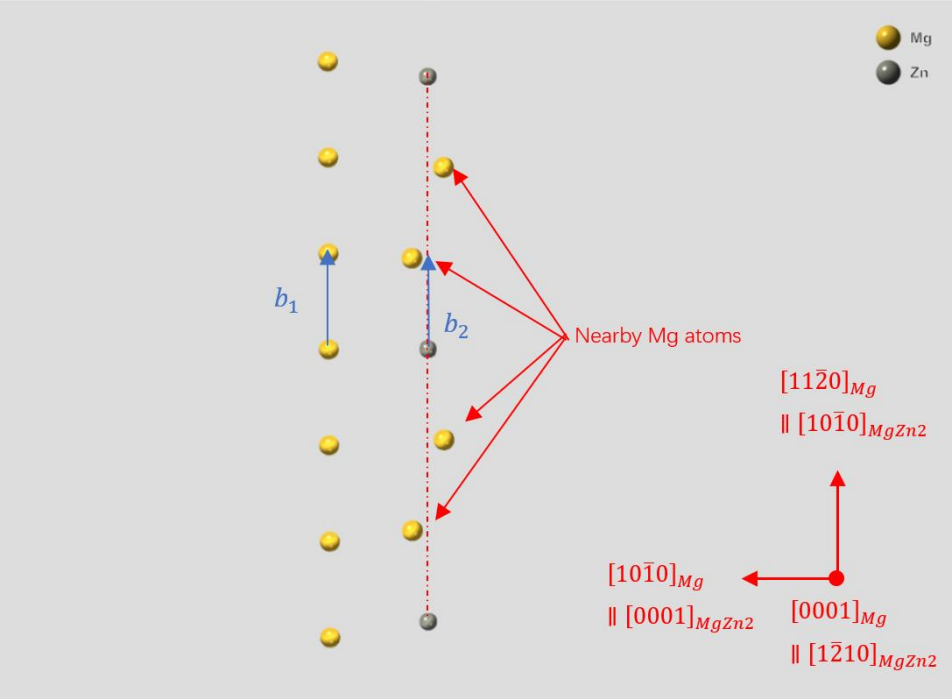

Figure 8 Schematic illustration showing the similarity of crystal structure between $[11\bar{2}0]_{Mg}$ and $[10\bar{1}0]_{MgZn2}$. With a suitable elastic strain, the interphase boundary could be semi-coherent or even coherent. The Burgers vectors are marked in the respective phases.

In order to show the interface in Figure 7 (which is $(1\bar{1}00)_{Mg} - (0001)_{MgZn2}$) more clearly, Figure 9 is reconstructed with the viewing direction along $[1\bar{1}00]_{Mg} \parallel [0001]_{MgZn2}$. The Mg atoms in the Mg matrix are coloured blue to enhance the contrast. With the Mg atoms near the $(0001)_{MgZn2}$ plane on the interface, ordered periodic near-coincident sites (marked with red circles) can be found throughout the

interface, which indicates that the crystal structures of the two phases on the interface are very similar.

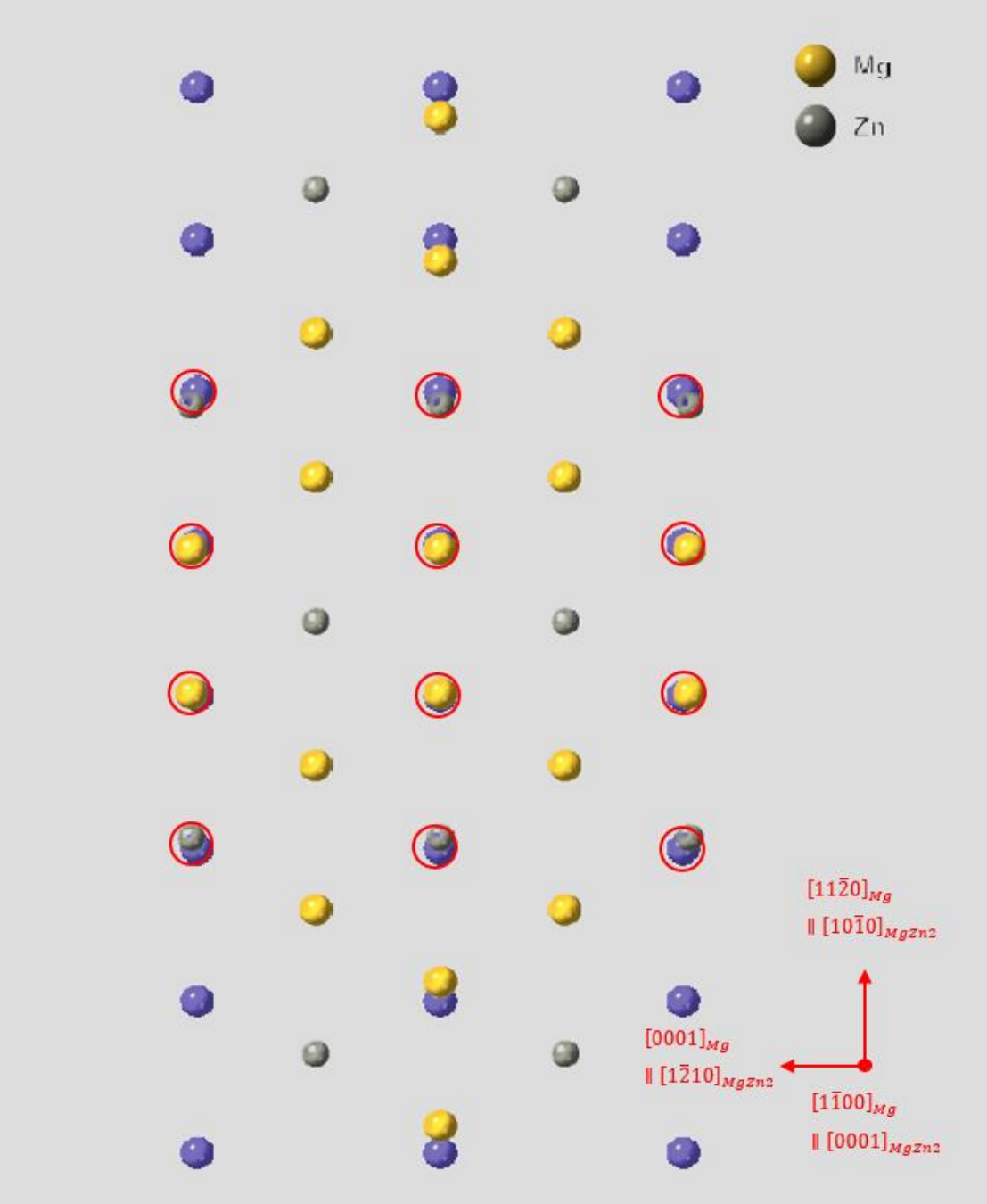

Figure 9 An illustration of the $(1\bar{1}00)_{Mg} - (0001)_{MgZn2}$ interface. The near-coincident sites are marked with red circles. The Mg atoms in the Mg matrix are coloured blue for better contrast

In addition, it should be noted that $\frac{1}{3}\langle 11\bar{2}0\rangle_{Mg}$ (b_1 in Figure 8) is a perfect vector in Mg, but the similar vector $\frac{1}{6}\langle 10\bar{1}0\rangle_{MgZn2}$ (b_2 in Figure 8) is not a perfect vector in $MgZn_2$. The motion of a single dislocation with the Burgers vector b_2 in $MgZn_2$ will create an APB behind it, requiring a group of three

together to maintain the crystal periodicity.

Therefore, with a semi-coherent or coherent interphase boundary, the Burgers vector of the basal **a** dislocations will remain nearly the same throughout the matrix and the $MgZn_2$ precipitate. On the other hand, with a similar shear modulus to that of $MgZn_2$ but with a much higher mismatch on the interface, c-axis Mg_2Sn rods in the Mg-6Sn-3Al alloy were not sheared. This again supports the idea that the coherency of the interphase boundary plays an important role in the transition from precipitate shearing to Orowan looping. Therefore, basal dislocations will face less resistance travelling into the precipitate, which could be the reason for the $MgZn_2$ precipitates being sheared.

4.2 Work-hardening in the Mg-6Sn-3Zn alloy

It can be found for the Mg-6Sn-3Zn alloy that, even considering all the strengthening mechanisms, including solid solution strengthening, Orowan strengthening and precipitate shearing, the estimated strength is still lower than that of the actually measured 29.92MPa. In addition, pillar compression tests have revealed an enormous work-hardening rate in the Mg-6Sn-3Zn alloy compared with Mg-6Sn and Mg-6Sn-3Al. The average work-hardening rates of 10% strain from all three Mg-Sn alloys are shown in Figure 10:

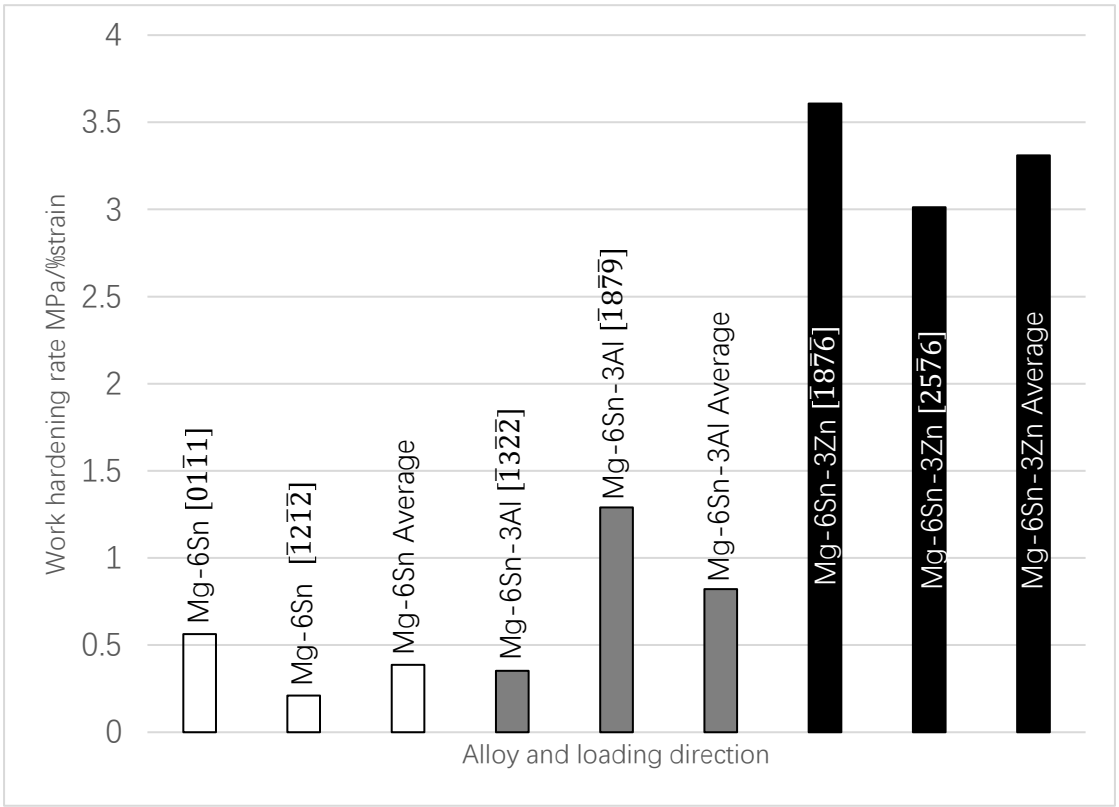

Figure 10 Work hardening rates of three Mg-Sn alloys with their respective loading directions

Work hardening is the increase in strength of metal due to blocking or cross slipping of dislocations preventing further dislocation motion [42]. For a precipitate strengthened alloy, the work hardening will be related to its precipitates. Assuming precipitates do not exist in the alloy, dislocations may glide freely within the alloys in groups and eliminate on the sample surface forming slip bands. With the existence of precipitates, the leading dislocations will be stopped at the precipitates which serve as a barrier. Therefore, succeeding dislocations will then pile up behind the leading dislocations and result in work hardening [43].

The high work-hardening rate from the Mg-6Sn-3Zn alloy is contributed by both the Mg_2Sn and the $MgZn_2$ precipitates. For the Mg_2Sn precipitates, comparing the Mg-6Sn and Mg-6Sn-3Al alloys, as indicated by Figure 10, the non-basal precipitates (Type 5 and Type 6 in Mg-6Sn-3Al) have increased the work-hardening rate due to more basal $\mathbf{a}$ dislocations being blocked and piling up at the precipitate-matrix interface which therefore resists further dislocation motion and promotes buckling and cross slip. The non-basal Mg_2Sn laths (Type 7 prismatic laths) will exhibit the same behaviour as the non-basal precipitates in the Mg-6Sn-3Al alloy. This would contribute to part of the strengthening and work hardening.

The $MgZn_2$ precipitates which are sheared during the slip are believed to be another main contributor to work hardening in the Mg-6Sn-3Zn alloy, which is different from Mg-6Sn and Mg-6Sn-3Al. As suggested by Alizadeh and Llorca, basal $\mathbf{a}$ dislocations have to pile up at the $MgZn_2$ precipitate-matrix interface before they can shear through the precipitate[44]. First-principles simulations of precipitates in Mg-Al alloys of the stacking fault energy indicate that a high stress is required to promote dislocation slip through the $Mg_{17}Al_{12}$ [45]. With multiple dislocations piling up prior to the dislocations penetrating the precipitates, stress is accumulated. This is also confirmed by Huang *et al.* on the shearable β_1 precipitates in Mg-RE alloys along with the simulation of Esteban-Manzanares *et al.* of the Mg-Al alloy system[46], [47]. The main reason for the enormous work hardening in the Mg-6Sn-3Zn alloy may lie in the finely distributed c-axis $MgZn_2$ narrow rods with a very high number density (contributing 78.60% of the entire precipitate population) and aspect ratio (~ 50:1). Therefore, fine and homogeneously distributed dislocation barriers will be present in the alloy. These barriers will then prevent further dislocation motion and lead to a great contribution to work hardening.

Hence, the high strength and work hardening of the Mg-6Sn-3Zn alloys are contributed by the stress accumulation from both the Orowan looping around the non-basal Mg_2Sn precipitates and the shearing of the $MgZn_2$ precipitates; the $MgZn_2$ precipitates are believed to be the main contributor.

5 Conclusion

In summary, a general modification of the Orowan strengthening equation has been proposed as an attempt to quantify accurately the contribution of different precipitate types to the CRSS of basal slip in multiple precipitate type systems. The modified Orowan model has been applied to the precipitate strengthening in the Mg-6Sn, Mg-6S-3Al and Mg-6Sn-3Zn alloys with multiple precipitate types. Although does not represent an exact solution, the suggested approach does appear to predict the strengthening in the three alloys we have studied sufficiently well, while retaining the simplicity and directness of earlier formulations (e.g. [25]).

Micro-pillar compression tests designed to activate basal slip have determined the CRSSs of the Mg-6Sn, Mg-6S-3Al and Mg-6Sn-3Zn alloys as 13.22MPa, 21.34MPa and 29.92MPa, respectively. Taking into account the basic strength of Mg, the contribution from Orowan strengthening, the solid solution strengthening and the precipitate shearing, the as-estimated CRSSs are 11.57MPa, 21.88MPa and 24.55MPa. For the Mg-6Sn and the Mg-6Sn-3Al alloys, the estimated results agree adequately with the experimental values. The gap between the as-estimated results and the experimentally measured result in Mg-6Sn-3Zn could be caused by stress accumulation from the precipitates.

6 Acknowledgments

The first author is grateful for financial support from the Chinese Scholarship Council (CSC) and the University of Birmingham.

7 References

[1] A. Srinivasan, K. K. Ajithkumar, J. Swaminathan, U. T. S. Pillai, and B. C. Pai, "Creep Behavior of AZ91 Magnesium Alloy," *Procedia Eng.*, vol. 55, pp. 109–113, 2013, doi: 10.1016/j.proeng.2013.03.228.

[2] C. J. Bettles, M. A. Gibson, and S. M. Zhu, "Microstructure and mechanical behaviour of an elevated temperature Mg-rare earth based alloy," *Mater. Sci. Eng. A*, vol. 505, no. 1–2, pp. 6–12, 2009, doi: 10.1016/j.msea.2008.11.004.

[3] S. M. Zhu, M. A. Gibson, M. A. Easton, and J. F. Nie, "The relationship between microstructure and creep resistance in die-cast magnesium-rare earth alloys," *Scr. Mater.*, vol. 63, no. 7, pp. 698–703, 2010, doi: 10.1016/j.scriptamat.2010.02.005.

[4] P. Poddar, K. L. Sahoo, S. Mukherjee, and A. K. Ray, "Creep behaviour of Mg–8% Sn and Mg–8% Sn–3% Al–1% Si alloys," *Mater. Sci. Eng. A*, vol. 545, pp. 103–110, 2012, doi: 10.1016/j.msea.2012.03.007.

[5] S. Ong, W. Richards, A. Jain, G. Hautier, M. Kocher, S. Cholia, D. Gunter, V. Chevrier, K. Persson, and G. Ceder, "Python Materials Genomics (pymatgen): A robust, open-source python library for materials analysis," *Comput. Mater. Sci.*, vol. 68, pp. 314–319, 2013, doi: https://doi.org/10.1016/j.commatsci.2012.10.028.

[6] C. Q. Liu, H. W. Chen, H. Liu, X. J. Zhao, and J. F. Nie, "Metastable precipitate phases in Mg–9.8 wt%Sn alloy," *Acta Mater.*, vol. 144, pp. 590–600, 2018, doi: 10.1016/j.actamat.2017.10.023.

[7] S. Henes and V. Gerold, "Rontgenographische Untersuchungen der Ausscheidungvorgange in Magnesium-Blei- und Magnesium-Zinn-Legierungen," *Zeitschrift für Met.*, vol. 53, p. 703, 1962.

[8] R. S. Busk, "Magnesium and Its Alloys," in *Handbook of Materials Selection*, John Wiley & Sons, Inc., 2002, pp. 259–265. doi: 10.1002/9780470172551.ch8.

[9] M. Gupta and N. M. L. Sharon, "Introduction to Magnesium," in *Magnesium, Magnesium Alloys, and Magnesium Composites*, John Wiley & Sons, Inc., 2011, pp. 1–12. doi: 10.1002/9780470905098.ch1.

[10] T. T. Sasaki, F. R. Elsayed, T. Nakata, T. Ohkubo, S. Kamado, and K. Hono, "Strong and ductile heat-treatable Mg-Sn-Zn-Al wrought alloys," *Acta Mater.*, vol. 99, pp. 176–186, 2015, doi:

10.1016/j.actamat.2015.06.060.

[11] T. T. Sasaki, K. Oh-ishi, T. Ohkubo, and K. Hono, “Enhanced age hardening response by the addition of Zn in Mg–Sn alloys,” *Scr. Mater.*, vol. 55, no. 3, pp. 251–254, 2006, doi: 10.1016/j.scriptamat.2006.04.005.

[12] T. T. Sasaki, J. D. Ju, K. Hono, and K. S. Shin, “Heat-treatable Mg-Sn-Zn wrought alloy,” *Scr. Mater.*, vol. 61, no. 1, pp. 80–83, 2009, doi: 10.1016/j.scriptamat.2009.03.014.

[13] Z. Z. Shi and W. Z. Zhang, “Newly observed prismatic Mg2Sn laths in a Mg-Sn-Zn-Mn alloy,” *J. Mater. Sci.*, vol. 48, no. 21, pp. 7551–7556, 2013, doi: 10.1007/s10853-013-7570-8.

[14] F. R. Elsayed, T. T. Sasaki, C. L. Mendis, T. Ohkubo, and K. Hono, “Compositional optimization of Mg-Sn-Al alloys for higher age hardening response,” *Mater. Sci. Eng. A*, vol. 566, pp. 22–29, 2013, doi: 10.1016/j.msea.2012.12.041.

[15] G. Douglas, “Microstructural Characterisation and Modelling of Dilute Magnesium -Tin -Aluminium Alloys,” University of Birmingham, 2017.

[16] Zhaoqian Sun, “Study on the Effect of Sn and Al Content on the Microstructure and Properties of the Mg-Sn-Al Alloys,” General Research Institute for Nonferrous Metals, 2021.

[17] C. Liu, H. Chen, and J.-F. Nie, “Interphase boundary segregation of Zn in Mg-Sn-Zn alloys,” *Scr. Mater.*, vol. 123, pp. 5–8, Oct. 2016, doi: 10.1016/j.scriptamat.2016.05.035.

[18] C. L. Mendis, C. J. Bettles, M. A. Gibson, and C. R. Hutchinson, “An enhanced age hardening response in Mg-Sn based alloys containing Zn,” *Mater. Sci. Eng. A*, vol. 435–436, pp. 163–171, 2006, doi: 10.1016/j.msea.2006.07.090.

[19] F. R. Elsayed, T. T. Sasaki, C. L. Mendis, T. Ohkubo, and K. Hono, “Significant enhancement of the age-hardening response in Mg-10Sn-3Al-1Zn alloy by Na microalloying,” *Scr. Mater.*, vol. 68, no. 10, pp. 797–800, 2013, doi: 10.1016/j.scriptamat.2013.01.032.

[20] H. Pan, G. Qin, M. Xu, H. Fu, Y. Ren, F. Pan, Z. Gao, C. Zhao, Q. Yang, J. She, and B. Song, “Enhancing mechanical properties of Mg-Sn alloys by combining addition of Ca and Zn,” *Mater. Des.*, vol. 83, pp. 736–744, 2015, doi: 10.1016/j.matdes.2015.06.032.

[21] Y. Chen, L. Jin, W. Li, Y. Song, and L. Hao, “Microstructure and mechanical properties of as aged Mg–3Sn–1Al and Mg–3Sn–2Zn–1Al alloy,” *Mater. Sci. Technol.*, vol. 31, no. 1, pp. 73–78, 2015, doi: 10.1179/1743284714Y.0000000607.

[22] F. S. Pan, S. Q. Luo, A. T. Tang, J. Peng, and Y. Lu, “Influence of stacking fault energy on formation of

long period stacking ordered structures in Mg-Zn-Y-Zr alloys," *Prog. Nat. Sci. Mater. Int.*, vol. 21, no. 6, pp. 485–490, 2011, doi: 10.1016/S1002-0071(12)60087-2.

[23] A. Vaid, J. Guénolé, A. Prakash, S. Korte-Kerzel, and E. Bitzek, "Atomistic simulations of basal dislocations in Mg interacting with Mg17Al12 precipitates," *Materialia*, vol. 7, no. May, p. 100355, 2019, doi: 10.1016/j.mtla.2019.100355.

[24] M. Gharghouri, G. C. Weatherly, J. D. Embury, and J. Root, "Study of the mechanical properties of Mg-7.7at.% Al by in-situ neutron diffraction," *Philos. Mag. A*, vol. 79, no. 7, pp. 1671–1695, 1999, doi: 10.1080/01418619908210386.

[25] J. F. Nie, "Effects of precipitate shape and orientation on dispersion strengthening in magnesium alloys," *Scr. Mater.*, vol. 48, no. 8, pp. 1009–1015, 2003, doi: 10.1016/S1359-6462(02)00497-9.

[26] C. Caceres and D. Rovera, "Solid solution strengthening in concentrated Mg-Al alloys," *J. Light Met.*, vol. 1, no. 3, pp. 151–156, 2001, doi: 10.1016/S1471-5317(01)00008-6.

[27] B. Q. Shi, R. S. Chen, and W. Ke, "Solid solution strengthening in polycrystals of Mg-Sn binary alloys," *J. Alloys Compd.*, vol. 509, no. 7, pp. 3357–3362, 2011, doi: 10.1016/j.jallcom.2010.12.065.

[28] A. Akhtar and E. Teghtsoonian, "Substitutional solution hardening of magnesium single crystals," *Philos. Mag.*, vol. 25, no. 4, pp. 897–916, 1972, doi: 10.1080/14786437208229311.

[29] A. Tehranchi, B. Yin, and W. A. Curtin, "Solute strengthening of basal slip in Mg alloys," *Acta Mater.*, vol. 151, pp. 56–66, 2018, doi: 10.1016/j.actamat.2018.02.056.

[30] Chris Schuh, "3.40J Physical Metallurgy." Massachusetts Institute of Technology: MIT OpenCourseWare, 2009.

[31] W. D. Robertson and R. E. Reed-Hill, "Additional modes of deformation twinning in magnesium," *Acta Metall.*, vol. 5, no. 12, pp. 717–727, 1957.

[32] A. Akhtar and E. Teghtsoonian, "Solid solution strengthening of magnesium single crystals-I alloying behaviour in basal slip," *Acta Metall.*, vol. 17, no. 11, pp. 1339–1349, 1969, doi: 10.1016/0001-6160(69)90151-5.

[33] H. Conrad and W. D. Robertson, "Effect of temperature on the flow stress and strain-hardening coefficient of magnesium single crystals," *JOM*, vol. 9, no. 4, pp. 503–512, 1957, doi: 10.1007/BF03397908.

[34] C. P. Blankenship, E. Hornbogen, and E. A. Starke, "Predicting slip behavior in alloys containing shearable and strong particles," *Mater. Sci. Eng. A*, vol. 169, no. 1–2, pp. 33–41, 1993, doi:

10.1016/0921-5093(93)90596-7.

[35] C. R. Hutchinson, J. F. Nie, and S. Gorsse, “Modeling the precipitation processes and strengthening mechanisms in a Mg-Al-(Zn) AZ91 alloy,” *Metall. Mater. Trans. A*, vol. 36, no. 8, pp. 2093–2105, 2005, doi: 10.1007/s11661-005-0330-x.

[36] M. Liao, B. Li, and M. F. Horstemeyer, “Interaction between prismatic slip and a Mg17Al12 precipitate in magnesium,” *Comput. Mater. Sci.*, vol. 79, pp. 534–539, 2013, doi: 10.1016/j.commatsci.2013.07.016.

[37] C. M. Cepeda-Jiménez, M. Castillo-Rodríguez, and M. T. Pérez-Prado, “Origin of the low precipitation hardening in magnesium alloys,” *Acta Mater.*, vol. 165, pp. 164–176, 2019, doi: 10.1016/j.actamat.2018.11.044.

[38] E. L. S. Solomon and E. A. Marquis, “Deformation behavior of β′ and β‴ precipitates in Mg-RE alloys,” *Mater. Lett.*, vol. 216, pp. 67–69, 2018, doi: 10.1016/j.matlet.2017.12.149.

[39] J. Wang and N. Stanford, “Investigation of precipitate hardening of slip and twinning in Mg5%Zn by micropillar compression,” *Acta Mater.*, 2015, doi: 10.1016/j.actamat.2015.08.012.

[40] W. D. Callister and D. G. Rethwisch, *Materials science and engineering: an introduction*, vol. 7. Wiley New York, 2007.

[41] C. S. Ltd, “CrystalMaker®.”

[42] L. M. Brown, “Strengthening Mechanisms in Crystal Plasticity, by Ali Argon,” *Contemp. Phys.*, vol. 54, no. 6, pp. 306–307, Nov. 2013, doi: 10.1080/00107514.2013.857723.

[43] D. Hull and D. J. Bacon, “Chapter 9 - Dislocation Arrays and Crystal Boundaries,” D. Hull and D. J. B. T.-I. to D. (Fifth E. Bacon, Eds. Oxford: Butterworth-Heinemann, 2011, pp. 171–204. doi: https://doi.org/10.1016/B978-0-08-096672-4.00009-8.

[44] R. Alizadeh and J. Llorca, “Interactions between basal dislocations and β1′ precipitates in Mg–4Zn alloy: Mechanisms and strengthening,” *Acta Mater.*, vol. 186, pp. 475–486, 2020, doi: 10.1016/j.actamat.2020.01.028.

[45] W. Xiao, X. Zhang, W. T. Geng, and G. Lu, “Atomistic study of plastic deformation in Mg-Al alloys,” *Mater. Sci. Eng. A*, vol. 586, pp. 245–252, 2013, doi: 10.1016/j.msea.2013.07.093.

[46] Z. Huang, C. Yang, L. Qi, J. E. Allison, and A. Misra, “Dislocation pile-ups at β1 precipitate interfaces in Mg-rare earth (RE) alloys,” *Mater. Sci. Eng. A*, vol. 742, no. September 2018, pp. 278–286, 2019, doi: 10.1016/j.msea.2018.10.104.

[47] G. Esteban-Manzanares, A. Ma, I. Papadimitriou, E. Martínez, and J. Llorca, “Basal dislocation/precipitate interactions in Mg-Al alloys: an atomistic investigation,” *Model. Simul. Mater. Sci. Eng.*, vol. 27, no. 7, 2019, doi: 10.1088/1361-651X/ab2de0.